Nanoscale

Accepted Manuscript

This article can be cited before page numbers have been issued, to do this please use: M. Du, L. Cui, P. Wang, C. Niu, Y. S. Kang and X. L. Zhang, *Nanoscale*, 2023, DOI: 10.1039/D3NR03477A.

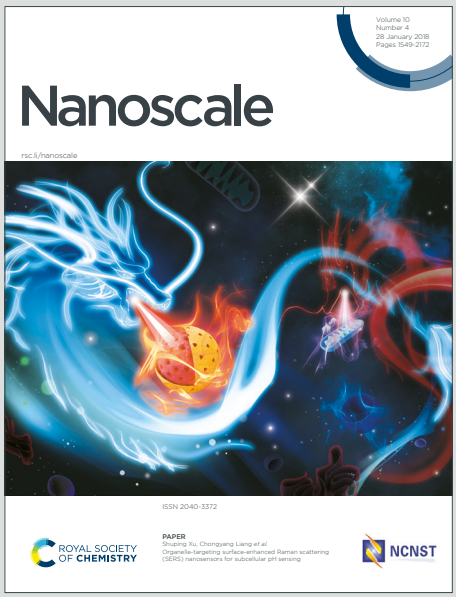

ROYAL SOCIETY OF CHEMISTRY

rsc.li/nanoscale

View Article Online
DOI: 10.1039/D3NR03477A

ARTICLE

Synergistic Material Modifications Induced Optimization of Interfacial Charge Transfer and Surface Hydrogen Adsorption

Received 00th January 20xx,
Accepted 00th January 20xx

DOI: 10.1039/x0xx00000x

Mingyan Du,[a,†] Lingling Cui,[a,†] Panpan Wang,[b,†] Chunyao Niu,[b,*] Young Soo Kang[c] and Xiao Li Zhang[a,*]

Being resourceful, chemically stable, and low cost, titanium dioxide (TiO_2) possesses the most desired advantages for photocatalytic applications. However, the intrinsic limits of high surface hydrogen adsorption energy, wide band gap, low separation rate and rapid recombination of the photogenerated charge carrier greatly hamper its utilization. To address the issues, the present work combines density function theory (DFT) calculations with rational modifications of TiO_2 with nickel doping and of an ultra-thin shield of fluorinated carbon (FNT) for application in the photocatalytic hydrogen evolution reaction (HER). Comprehensive studies imply that the synergistic modifications not only optimize the surface H adsorption but also facilitate the interfacial charge transfer and simultaneously prevent the photochemical and chemical corrosion of the catalysts. Well agreeing with the theoretical preview, the resulted FNT photocatalysts demonstrate an optimal HER efficiency of 13.0 $mmol \cdot g^{-1} \cdot h^{-1}$, nearly 33-times and over three-times beyond that of the pristine TiO_2 (0.4 $mmol \cdot g^{-1} \cdot h^{-1}$) and the Ni-doped TiO_2 (4.2 $mmol \cdot g^{-1} \cdot h^{-1}$), respectively. Moreover, the composite also exhibits excellent stability with well-reproduced HER performance over a 66-hour cyclic HER test of 15 cycles.

Introduction

Artificial solar fuel generation is an encouraging route toward a carbon-neutral future because it can produce value-added chemicals and fuels while storing the vastly available clean energy of sunlight.[1-5] A typical, well recognized, chemically stable, and low-price semiconductor, titanium dioxide is widely used as an earth-abundant component in the photocatalytic H_2 evolution reaction (HER).[6-8] The intrinsic bandgap of 3.0-3.2 eV makes it difficult to respond to the visible range of solar irradiation. Undesired high surface hydrogen adsorption energy and rapid recombination of the photogenerated charges also determine strategic material engineering to meet the requirements for the photocatalytic application.[9]

Conventional studies on modifications such as doping and coating to enable some adequate alterations to the chemical and electrical properties of TiO_2 have been focused on widening the photoactivity response window, retarding the recombination of charge carriers, and cost-effectiveness in contrast to the precious elements Ag, Au, and Pt, etc.[10-13] For instance, high reserve transition metals (e.g., Fe, Co, Ni, and Al) with close ionic radii to Ti that allow successful implantation into the lattice of TiO_2 have been widely studied.[14] The strong electronic interaction between the transition metal atoms (such as Ni) and TiO_2 promotes the formation of Ti^{3+}/O_V (oxygen vacancy) configuration[15] and the generation of Ti^{3+} species, benefiting charge compensation and the formation of oxygen vacancy.[16] The synergistic effect of bi-Ti^{3+} and O_V is responsible for the high photocatalytic activity by prompting charge transfer and retarding recombination.[1, 16, 17].

Making use of the electrostatic attraction from a highly electronegative coating provides a facile and encouraging solution to direct the photogenerated electron flow, which establishes an efficient charge separation and transfer from the bulk to the surface and then participates in the photocatalytic reaction on the surface.[18] Carbon coating is one of the most promising surface modification approaches and possesses versatile properties including obtainability, high electric conductivity, and large electron storage capacity, as well as improving visible-light absorption and photoexcited electron transfer. More electronegative halogen atoms e.g. fluorine, holds the potential to strengthen the electronic interaction between TiO_2 and surface carbon layer and greatly further the interfacial electron transfer.[18-20]

Despite conventional studies, recent comprehensive experimental and theoretical studies have shown that the free energy of hydrogen adsorption (ΔG_{H^*}) on the catalyst surface is one of the governing HER activity indicators. An ideal HER catalyst has a moderate free energy of hydrogen adsorption ($\Delta G_{H^*} \approx 0$) according to the Sabatier principle, where the hydrogen is bound neither too strongly nor too weakly. Herein, combined computing simulation previews, material modifications and experimental characterizations were conducted to demonstrate rational band structural engineering and tune the surface hydrogen adsorption energy of the catalyst to boost photocatalytic HER performance. Agreeing well with the theoretical preview, the synergistic effects in the thin fluorinated-carbon encapsulated Ni-doped TiO_2 (FNT) enable an optimal photocatalytic HER of 13.0 $mmol \cdot g^{-1} \cdot h^{-1}$, nearly 33-times and over three-times to that of the pure TiO_2 (ca. 0.4 $mmol \cdot g^{-1} \cdot h^{-1}$) and the Ni-

[a.] School of Materials Science and Engineering, Zhengzhou University, 450001 P.R. China.
[b.] School of Physics and Microelectronics, Zhengzhou University, 450001 P.R. China.
[c.] Environmental and Climate Technology, Korea Institute of Energy Technology (KENTECH), 200 Hyeoksin-ro, Naju City, Jeollanamdo 58330, Korea.
† Equal contribution.
* Corresponding authors. E-mail: xiaolizhang.z@gmail.com
Electronic Supplementary Information (ESI) available: See DOI: 10.1039/x0xx00000x

View Article Online
DOI: 10.1039/D3NR03477D

doped TiO_2 (4.2 mmol·g^{-1}·h^{-1}), respectively. A cyclic HER measurement of 66 h and 15 cycles demonstrates excellent stability with steady HER performances. The thin fluorinated carbon shield not only optimizes the surface hydrogen adsorption but also escalates the interfacial charge transfer and serves as a physical protection layer to prohibit corrosion from the wet-chemical and photochemical environments, resulting in significantly improved photocatalytic HER ability.

Results and Discussions

Doping of external atoms and covering of highly conductive materials such as graphene are proven effective strategies to optimize the photocatalytic performance of TiO_2.[18, 21-24] For a preview of the HER activity and the mechanism behind it, density functional theory (DFT) computational estimations were conducted to investigate the effects of each modification approach (Ni doping, thin carbon shield, and fluorination of the carbon) on the HER activity of TiO_2. The highly stable TiO_2 (101) surface is used as the substrate throughout the simulation. Two interstitial sites are taken into account for Ni atom doping; see Figure S1, where $Ni_a@TiO_2$ is a more energetically favorable site (about 0.3 eV) and is chosen for the demonstration. To simplify the calculation, graphene is used to demonstrate the thin carbon shield on the TiO_2 composites. Therefore, four candidates, including TiO_2, $Ni_a@TiO_2$, graphene covered $Ni_a@TiO_2$ ($G/Ni_a@TiO_2$), and fluorinated graphene covered $Ni_a@TiO_2$ ($F\text{-}G/Ni_a@TiO_2$), are used in the calculations.

As a main descriptor, calculations on the adsorption energies of the H atom on both O and Ti sites are conducted, which suggest preferable adsorption on the O atom, as illustrated in Figure 1a. Pure TiO_2 has an endothermic ΔG_{H^*} of 0.61 eV implying almost inert HER ability (see Figure 1b), and Ni-doping lowers the ΔG_{H^*} to 0.53 eV, improving the HER activity of nearby O sites via doping. Graphene cover reduces the ΔG_{H^*} to 0.43 eV, further enhancing the HER activity. Interestingly, fluorine-doping significantly pushes the ΔG_{H^*} value of the graphene down to 0.15 eV, implying a dramatic development in HER activity due to the synergistic effects of Ni-doping, carbon shield, and further fluorine-doping of the thin carbon shield.

To gain insight into the underlying mechanism of HER activation, the differential charge density was analyzed to demonstrate the electron interaction between H* and active sites through the representation of the electron accumulation and dissipation with yellow and cyan colors, respectively, in Figure 1c. The adsorption of H atoms on O results in apparent partial charge redistribution via the formation of an O-H covalent bond. Ni-doping in TiO_2 increases the electron transfer and strengthens the interaction between H and O. The Bader charge analysis reveals an electron donation of 0.43 electrons from the Ni to the TiO_2, which slightly enhances the H adsorption capacity. After placing graphene over the $Ni_a@TiO_2$ surface, the interaction between H and graphene stabilizes the H at the interface. Fluorination furthers the electronic interaction between graphene and H, improving H bonding.

In addition, the partial density of states (PDOS, in Figure 1d) reveals the electronic properties of the four systems, where the pure TiO_2 has a large band gap. The Ni doping introduces impurity energy levels in the band gap and activates the inert TiO_2 surface, improving

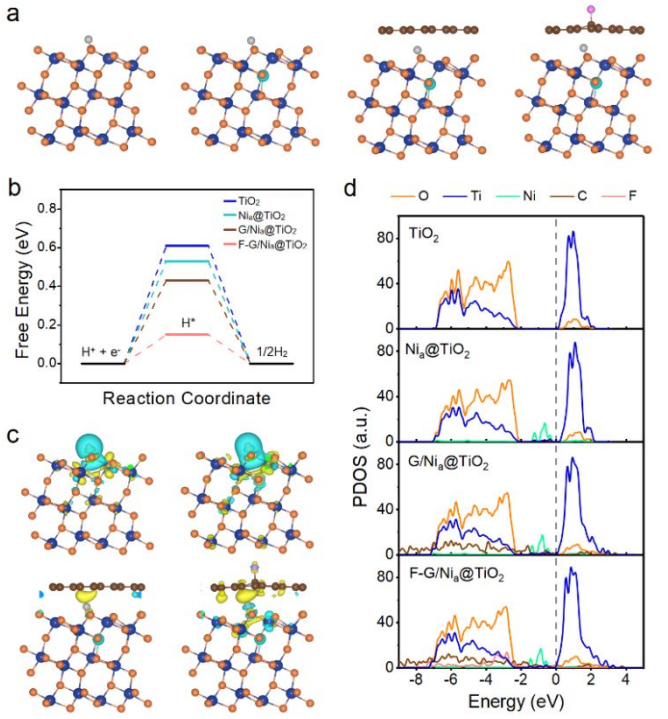

Fig. 1 (a) The most stable position for adsorption of H atoms on TiO_2, $Ni_a@TiO_2$, $G/Ni_a@TiO_2$, and $F\text{-}G/Ni_a@TiO_2$ (H, gray; Ti, navy blue; O, orange; Ni, green; C, brown; F, pink). (b) Free energy diagrams of HER on catalysts. (c) Charge density difference after H adsorption on catalysts (the isosurface value is 0.01 e/Å^3). (d) Projected density of states (PDOS) of catalysts (the CBM of TiO_2 is chosen as the zero energy reference point).

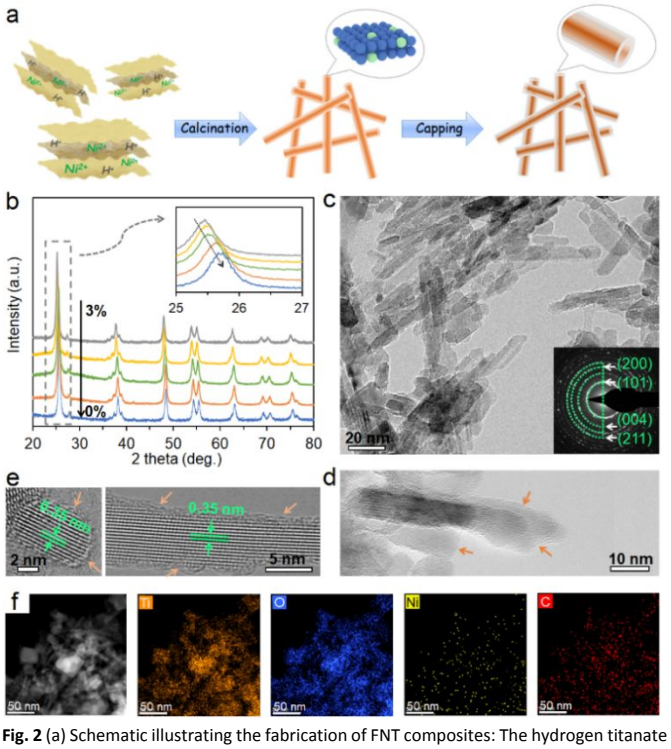

Fig. 2 (a) Schematic illustrating the fabrication of FNT composites: The hydrogen titanate with embedded Ni^{2+} is calcined in air, then encapsulated with carbon or fluorinated carbon. (b) XRD analyses (inset enlarged XRD patterns between 2ϑ of 25° to 27°) of the FNTx composites with varying Ni-doping levels. (c) TEM image (inset SAED pattern), (d-e) HR-TEM images, and (f) Element mapping analyses for Ti, O, Ni and C of FNT2 (2wt% Ni-doping), respectively.

its catalytic performance. Graphene cover leads to the energy states of graphene filling the TiO_2 band gap, and the interaction of the F atom with graphene creates more impurity states in the band gap. Following the development of new energy states in the TiO_2 band gap, the HER activity of the catalyst is gradually improved by optimizing the adsorption of H atoms and light absorption.

It has been reported that strongly adsorbed hydroxyl (OH*) and hydrogen (H*) on the active sites inhibit the HER process if not removed timely.[25–27] Corresponding adsorption energies of OH* and H* are presented in Table S1, showing different preferable adsorbing sites of the H* (on O sites) and OH* (on Ti sites) on TiO_2 surface, indicating negligible impact on the HER active site from the adsorption of OH. While the OH* can be easily removed through water-assisted mechanism.[26] Although the H coverage increase weakens the H* adsorption, the H binding strengths and the HER activity display well maintained trends.[28]

The process for fabricating the fluorinated-carbon coating on titanium dioxide with Ni-doping is schematically illustrated in Figure 2a, with a description of details in the supporting information. The doping effect on the crystalline structure was estimated using X-ray diffraction (XRD) analyses of the Ni-doped TiO_2 with different nickel contents (sample NTx). The main characteristic peaks of XRD (Figure S2d) can be ascribed to anatase TiO_2 (JCPDS card no. 21-1272), with a very small proportion of rutile TiO_2 (JCPDS card no. 21-1276). Increasing Ni substitute induces a peak shift to the lower angle, as shown in the enlarged area of the XRD between 2θ of 25-27° (inset of Figure S2d). Based on Bragg's law $2d\sin\theta=\lambda$, the phenomenon is attributed to the expanding inter-planar spacing of TiO_2 due to Ni-doping, confirming the successful implantation of Ni(II) into the TiO_2 lattice.[29, 30] Figure S2e, Raman spectra of the NTx, consists of four main peaks locating at 151, 203, 404, 519 and 644 cm^{-1} assigning them to the modes of $E_{g(1)}$, $E_{g(2)}$, $B_{1g(1)}$, $A_{1g}+B_{1g(2)}$, and $E_{g(3)}$ of anatase TiO_2, respectively.[31] The absorption fringe at about 380 nm of the corresponding UV-Vis spectra in Figure S2f reflects the band-edge of optical absorption of the TiO_2, which gradually shifts to a longer wavelength with the increase in nickel content.

Capping an ultrathin fluorinated carbon doesn't change the phenomenon of the monotonous XRD peak shift, as demonstrated by the sample FNTx in Figure 2b. Transmission electron microscopy (TEM) of the FNT2 composite, see Figure 2c, exhibits a maintained morphology of nanorods with negligible morphological variation from the NT2 (Figure S2a). Inset of Figure 2c is the corresponding selected area electron diffraction pattern (SAED) which consists of continuous rings assigned to the (101), (004), (200), and (211) crystal planes of anatase TiO_2.[32, 33] The fluorinated thin carbon shield is of approximately 1 nm in thickness and can be easily observed on the surface of the nanorods, which is pointed out by the arrows in Figure 2d and Figure 2e. The spacing of 0.35 nm between the two adjacent lattice facets can be indexed to the (101) crystalline facets of anatase, Figure 2e.[34] The morphological and crystalline characteristic information of FNT2 is consistent with that of NT2 (Figures S2b and Figure S2c), suggesting negligible influence on the morphology and crystal phase from the surface shield of the fluorinated carbon. Meanwhile, the element distribution mapping analyses (see Figure 2f) manifest the homogeneous distribution of Ti, O, Ni and C elements throughout the entire FNT2.

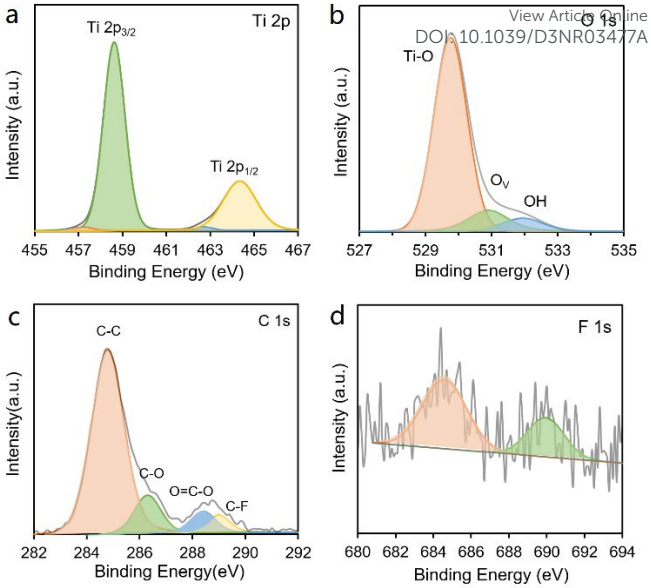

Fig. 3 XPS spectra of (a) Ti 2p, (b) O 1s, (c) C 1s and (d) F 1s of the FNT2 composite.

Aiming at an understanding of the influence of varying modifications, X-ray photoelectron spectroscopy (XPS) analyses were conducted to further elaborate on the relationship between the chemical composition and activity of the photocatalyst. In comparison to the NT2, fluorinated carbon wrapping on the surface further reduces the XPS signal of Ni elements. In Figure 3a, the Ti 2p photoelectron spectra of FNT2 can be fitted with four peaks, with the peaks located at 458.6 and 464.3 eV, respectively, corresponding to Ti $2p_{3/2}$ and Ti $2p_{1/2}$ core levels of Ti^{4+}. Two low-intensity peaks at 457.2 and 462.7 eV are attributed to the Ti^{3+} species, reflecting the existence of oxygen vacancies (O_V).[35-37] In addition, the absence of the Ti-C characteristic peak suggests a surface shield of the fluorine-adsorbed carbon instead of doping into the TiO_2 lattice, which is in good agreement with the XRD and TEM characterizations. Moreover, the formation of O_V is confirmed by the corresponding O 1s XPS spectra. Figure 3b shows lattice oxygen (labelled as Ti-O), oxygen vacancies (labelled as O_V), and foreign OH groups (labelled as OH) peaks centered at 529.7, 530.5, and 532.0 eV, respectively.[35, 38] Figure 3c is the high-resolution XPS spectrum of C 1s, which displays four typical peaks with binding energies of 284.8, 286.3, 288.4, and 288.9 eV belonging to C-C, C-O, O=C-O, and C-F, respectively.[18, 39, 40] In Figure 3d, two peaks are demodulated from the F 1s spectrum at 684.6 eV and 689.9 eV, ascribing them to semi-ionic and covalent C–F bonds, respectively. [41, 42]

In addition, the concentrations of Ti^{3+}, O_V, and OH from different modification processes are further estimated based on the peak areas of the Ti 2p and O 1s photoelectron spectra for TiO_2, NT2, CNT2, and FNT2 samples (see Figure S3 – Figure S5 and Figure 3) and summarized in Table S2. Introducing Ni into the TiO_2 lattice spontaneously increases the concentration of Ti^{3+}/O_V conformation,[37] which is then partially reduced after capping with the electronegative carbon or fluorinated carbon. While the surface hydroxyl groups show monotonous growth following the modification process. A suitable Ti^{3+}/O_V conformation concentration enables a progressive optimization of HER performance, promoting interfacial charge transfer, rather than functions as electron

recombining centers.[1] Meanwhile, the increasing surface hydroxyl groups on the catalyst compensates for the charge imbalance in the lattice caused by the substitution of Ti^{3+} for Ti^{4+} sites.[38, 43]

Photocatalytic HER measurement was conducted to evaluate the photocatalytic activity of the samples using a 10% aqueous methanol solution under the irradiation of a 300 W xenon lamp (Figure 4). Figure S6 reveals the influence of the Ni-doping on the HER performance of the NTx. Of all the samples, 2.0 wt% of Ni-doping leads to a maximum HER rate of 4.2 mmol·g^{-1}·h^{-1} (NT2), 10-fold higher than that of the pure TiO_2 (NT0) of 0.4 mmol·g^{-1}·h^{-1}. The clear enhancement can be derived from the increased H bonding ability and better charge separation induced by Ni-doping.[29, 40] Following modification of Ni-doped TiO_2 nanorods with a thin layer of electronegative carbon shield as shown in Figure S8, the resulted composite (CNT2) reaches an optimal HER efficiency of 10.3 mmol·g^{-1}·h^{-1} at a Ni: C ratio of 1: 1, implying significantly enhanced charge separation and transfer.

Figure 4b exhibits the development of the HER activity with a fluorinated thin carbon shield based on the investigation of an optimal carbon content in Figure S8. The HER efficiencies follow a same trend as the NTx (Figure S6) and the CNTx (Figure S7). Among the FNTx, FNT2 reaches an optimal HER efficiency of 13.0 mmol·g^{-1}·h^{-1}, which is nearly 33-fold and over 3-fold to that of the pure TiO_2 and the NT2, respectively, and a further 30% enhancement beyond the CNT2, as shown in Figure 4a. FNT2 shows an apparent quantum efficiency (AQE) of approximately 5.79% at a wavelength of 365nm, and a visible light HER of 0.528 mmol·g^{-1}·h^{-1} using a 420 nm cut-on filter. The high electronegativity of fluorine furthers the H adsorption ability as well as the electron transfer, thereby greatly contributing to the photocatalytic HER performance. A long-term cyclic HER test over 66 h consisting of 15 cycles was taken to assess the reproducibility of the HER and the stability of the composite, in Figure 4c. The FNT2 exhibits steady photocatalytic performance with a well-reproduced HER efficiency of approximately 13.0 mmol·g^{-1}·h^{-1}, confirming its superior photocatalytic HER activity and excellent

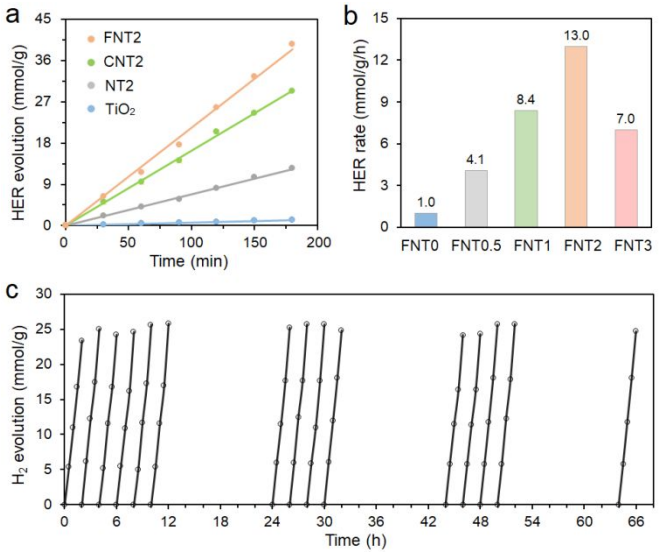

Fig. 4 (a) Hydrogen evolution measurements for pure TiO_2, NT2, CNT2, and FNT2; (b) HER rates for FNTx (FNT0 – FNT3); and (c) Cyclic HER (15 cycles over 66 h) of FNT2.

stability against wet-chemical and photochemical reactions. Table S3

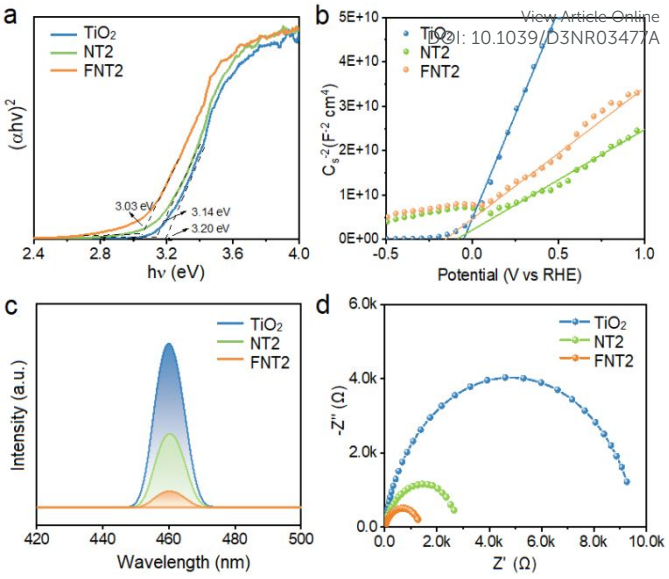

Fig. 5 (a) Tauc plots, (b) Mott-Schottky curves, (c) Photoluminescence spectra, and (d) Electrochemical impedance spectra of pure TiO_2, NT2, and FNT2 samples.

exhibits comparison photocatalytic HER recently reported metal-doped TiO_2 photocatalysts composites showing considerably high HER efficiency of the FNT2.

The presence of a high electronegative fluorinated carbon shield makes the FNT2 have better electronic structure and optoelectronic properties. In Figure S9, the UV-vis diffuse reflectance spectra of the NT2 and FNT2 samples demonstrate a significant broad background absorption in the visible range of 400-700 nm following the Ni-doping and surface shield of fluorinated carbon. In Figure 5a, the gradual narrowing of the band gap from 3.2 eV of TiO_2 to 3.1 eV of NT2 and then to 3.0 eV of FNT2 revealed by the Tauc plots reflects the aforementioned additional energy states in the band gap of TiO_2 from the various modifications. Comparison Mott-Schottky (MS) measurements, see Figure 5b, establish positive slopes of all three curves reflecting the unchanged n-type intrinsic nature of the samples from the modifications, which clearly exhibit flat band potential (vs. reversible hydrogen electrode, RHE) and a negative shift from -0.05 V of TiO_2 to -0.08 V of NT2 to -0.16 V of FNT2, respectively.[11, 45] Since the E_f of n-type semiconductors is typically about 0.1 – 0.3 V more positive than its conduction band minimum (CBM), the CBMs can be estimated as -0.35 V for TiO_2, -0.38 V for NT2, and -0.46 V for FNT2. The elucidated electronic band structures versus RHE at pH 7.0 by combining the UV-Vis and Mott-Schottky measurement results determine the narrowest band gap and a suitable energy band edge position of the sample FNT2, which is favorable to the HER reaction among the three samples, agreeing well with the theoretical preview.

The modifications also induce better charge separation and transfer. The number of electrons recombined with holes under photon emission was investigated using photoluminescence (PL) spectroscopy (Figure 5c).[46] All samples exhibit a strong fluorescence band centered at ca. 460 nm, with the highest PL intensity from pure TiO_2. Lower PL emission intensity reflects retarded carrier recombination and longer lifetimes of electron-hole pairs.[47] The FNT2 owns the lowest fluorescence intensity, suggesting superior photogenerated electron-hole pair separation and transfer, which

greatly contributes to the photocatalytic performance. Figure 5d shows the electrochemical impedance spectra (EIS) measuring the photocatalytic kinetics of the samples, where the smaller radius of the semicircle indicates faster electron transfer.[48, 49] Ni-doping effectively reduces the ohmic electric resistance (R_s) and charge transfer resistance (R_{ct}) of TiO_2. A fluorinated carbon shield significantly reduces the electron transfer resistance and furthers the effective charge transfer to participate in photocatalytic reactions on the catalyst surface.[44]

Conclusions

The synergistic modifications from Ni-doping, a thin carbon shield, and further fluorination induce new energy states into the TiO_2 band gap, enable a progressive optimization of the surface hydrogen adsorption, photogenerated charge carrier separation and interfacial charge transfer, and tune the Ti^{3+}/O_V conformation, the surface hydroxyl group and the photoactive wavelength region, resulting in the gradual development of the HER performance of the composites. The ultra-thin shield of fluorinated carbon on Ni-doped titanium dioxide (FNT) functions as not only an effective electron trapping layer but also a physical protection layer, greatly boosting the photocatalytic HER performance and stability. The resulted FNT photocatalysts demonstrated an optimal HER efficiency of 13.0 $mmol \cdot g^{-1} \cdot h^{-1}$ with excellent stability consisting of 15 cycles over 66 h, 33-fold the HER of pristine TiO_2.

Author Contributions

All authors have contributed to the preparation of the manuscript and given approval to the final version of the manuscript.

Conflicts of interest

All authors declare that they have no conflict of interest.

Acknowledgements

XLZ acknowledges the National Natural Science Foundation of China (NSFC, 51602291). CN acknowledges the Henan provincial key science and technology research project (No. 222102240023). YSK acknowledges the National Research Foundation of Korea (No. 2020R1A3B3079715).

References

1 M. Xiao, L. Zhang, B. Luo, M. Lyu, Z. Wang, H. Huang, S. Wang, A. Du and L. Wang, *Angew. Chem., Int. Ed.* , 2020, **59**, 7230 – 7234.
2 Z. Lin, C. Du, B. Yan, C. Wang and G. Yang, *Nat. Commun.*, 2018, **9**, 4036.
3 B. H. Lee, S. Park, M. Kim, A. K. Sinha, S. C. Lee, E. Jung, W. J. Chang, K. S. Lee, J. H. Kim, S. P. Cho, H. Kim, K. T. Nam and T. Hyeon, *Nat. Mater.*, 2019, **18**, 620-626.
4 Y. Ham, T. Hisatomi, Y. Goto, Y. Moriya, Y. Sakata, A. Yamakata, J. Kubota and K. Domen, *J. Mater. Chem. A*, 2016, **4**, 3027-3033.
5 N. Dubouis and A. Grimaud, *Chem. Sci.*, 2019, **10**, 9165-9181.
6 X. Zhang, Y. Chen, Y. Xiao, W. Zhou, G. Tian and H. Fu, *Nanoscale*, 2018, **10**, 4041-4050.
7 H. Wei, E. F. Rodriguez, A. F. Hollenkamp, A. I. Bhatt, D. Chen and R. A. Caruso, *Adv. Funct. Mater.*, 2017, **27**, 1703270.
8 A. Meng, L. Zhang, B. Cheng and J. Yu, *Adv. Mater.*, 2019, **31**, 1807660.
9 W. Zhang, H. He, H. Li, L. Duan, L. Zu, Y. Zhai, W. Li, L. Wang, H. Fu and D. Zhao, *Adv. Energy Mater.*, 2020, **11**, 2003303.
10 J. Y. Kim, S. Rhee, H. Lee, K. An, S. Biswas, Y. Lee, J. W. Shim, C. Lee and H. Kim, *Adv. Mater. Interfaces*, 2020, **7**, 1902003.
11 J. K. Kim, S. U. Chai, Y. Ji, B. Levy-Wendt, S. H. Kim, Y. Yi, T. F. Heinz, J. K. Nørskov, J. H. Park and X. Zheng, *Adv. Energy Mater.*, 2018, **8**, 1801717.
12 B. Guan, J. Yu, S. Guo, S. Yu and S. Han, *Nanoscale Adv.*, 2020, **2**, 1352-1357.
13 S. George, S. Pokhrel, Z. Ji, B. L. Henderson, T. Xia, L. Li, J. I. Zink, A. E. Nel and L. Mädler, *J. Am. Chem. Soc.*, 2011, **133**, 11270-11278.
14 M. Baruah, S. L. Ezung, S. Sharma, U. B. Sinha and D. Sinha, *Inorg. Chem. Commun.*, 2022, **144**, 109905.
15 M. Xu, S. He, H. Chen, G. Cui, L. Zheng, B. Wang and M. Wei, *ACS Catal.*, 2017, **7**, 7600-7609.
16 X. Bi, G. Du, A. Kalam, D. Sun, Y. Yu, Q. Su, B. Xu and A. G. Al-Sehemi, *Chem. Eng. Sci.*, 2021, **234**, 116440.
17 Y. Xu, T. F. Tay, L. Cui, J. Fan, C. Niu, D. Chen, Z. X. Guo, C. Sun, X. L. Zhang and R. A. Caruso, *Inorg. Chem.*, 2020, **59**, 17631-17637.
18 H. Song, J. Yu, Z. Tang, B. Yang and S. Lu, *Adv. Energy Mater.*, 2022, **12**, 2102573.
19 D. Y. Shin, K. W. Sung and H. J. Ahn, *Chem. Eng. J.*, 2021, **413**, 127563.
20 R. Hailili, C. Wang and E. Lichtfouse, *Appl. Catal. B*, 2018, **232**, 531-543.
21 J. Zhang, W. Xiao, P. Xi, S. Xi, Y. Du, D. Gao and J. Ding, *ACS Energy Lett.*, 2017, **2**, 1022-1028.
22 S. A. Shah, X. Shen, M. Xie, G. Zhu, Z. Ji, H. Zhou, K. Xu, X. Yue, A. Yuan, J. Zhu and Y. Chen, *Small*, 2019, **15**, 1804545.
23 C. Liu, D. Hao, J. Ye, S. Ye, F. Zhou, H. Xie, G. Qin, J. Xu, J. Liu, S. Li and C. Sun, *Adv. Energy Mater.*, 2023, **13**, 2204126.
24 L. Ferrighi, M. Datteo, G. Fazio and C. D. Valentin, *J. Am. Chem. Soc.*, 2016, **138**, 7365-7376.
25 I. T. McCrum and M. T. M. Koper, *Nat. Energy*, 2020, **5**, 891–899.
26 H. Q. Fu, M. Zhou, P. F. Liu, P. Liu, H. Yin, K. Z. Sun, H. G. Yang, M. Al-Mamun, P. Hu, H. F. Wang and H. Zhao, *J. Am. Chem. Soc.*, 2022, **144**, 6028–6039.
27 T. J. Schmidt, P. N. Ross Jr and N. M. Markovic, *J. Electroanal. Chem*., 2002, **524-525**, 252-260
28 H. Li, J. Xiao, Q. Fu and X. Bao, *Proc. Natl. Acad. Sci. U.S.A.*, 2017, **114**, 5930–5934.
29 Y. Yan, X. Lang, L. Li, T. Xu, P. Sun and K. Cai, Int. J. Energy Res., 2021, **45**, 15577-15585.
30 M. C. Tsai, T. T. Nguyen, N. G. Akalework, C. J. Pan, J. Rick, Y. F. Liao, W. N. Su and B. J. Hwang, *ACS Catal.*, 2016, **6**, 6551-6559.
31 R. J. G. Nuguid, D. Ferri, A. Marberger, M. Nachtegaal and O. Kröcher, *ACS Catal.*, 2019, **9**, 6814-6820.

View Article Online
DOI: 10.1039/D3NR03477A

32 Z. Li, Q. Zhou, J. Liang, L. Zhang, X. Fan, D. Zhao, Z. Cai, J. Li, D. Zheng, X. He, Y. Luo, Y. Wang, B. Ying, H. Yan, S. Sun, J. Zhang, A. A. Alshehri, F. Gong, Y. Zheng and X. Sun, *Small*, 2023, **19**, 2300291.

33 W. Wang, D. Zhu, Z. Shen, J. Peng, J. Luo and X. Liu, *Ind. Eng. Chem. Res.*, 2016, **55**, 6373-6383.

34 S. Song, H. Song, L. Li, S. Wang, W. Chu, K. Peng, X. Meng, Q. Wang, B. Deng, Q. Liu, Z. Wang, Y. Weng, H. Hu, H. Lin, T. Kako and J. Ye, *Nat. Catal.*, 2021, **4**, 1032-1042.

35 J. Zhao, B. Wang, Y. Zhao, M. Hou, C. Xin, Q. Li and X. Yu, *J. Phys. Chem. Solids*, 2023, **179**, 111374.

36 S. Tan, Z. Xing, J. Zhang, Z. Li, X. Wu, J. Cui, J. Kuang, Q. Zhu and W. Zhou, *J. Catal.*, 2018, **357**, 90-99.

37 H. Peng, T. Yang, H. Lin, Y. Xu, Z. Wang, Q. Zhang, S. Liu, H. Geng, L. Gu, C. Wang, X. Fan, W. Chen and X. Huang, *Adv. Energy Mater.*, 2022, **12**, 2201688.

38 G. Wang, J. Zheng, H. Bi, S. Wang, J. Wang, J. Sun, Y. Guo and C. Wang, *Scr. Mater.*, 2019, **162**, 28-32.

39 L. Zhao, X. Chen, X. Wang, Y. Zhang, W. Wei, Y. Sun, M. Antonietti and M. M. Titirici, *Adv. Mater.*, 2010, **22**, 3317-3321.

40 C. Chen, A. Wu, H. Yan, Y. Xiao, C. Tian and H. Fu, *Chem. Sci.*, 2018, **9**, 4746-4755.

41 D. Y. Shin and H. J. Ahn, *ACS Appl. Mater. Interfaces*, 2020, **12**, 19210-19217.

42 W. He, L. Han, Q. Hao, X. Zheng, Y. Li, J. Zhang, C. Liu, H. Liu and H. L. Xin, *ACS Energy Lett.*, 2019, **4**, 2905-2912.

43 A. Kusior, J. Banas, A. Trenczek-Zajac, P. Zubrzycka, A. Micek-Ilnicka and M. Radecka, *J. Mol. Struct.*, 2018, **1157**, 327-336.

44 W. Zhang, Y. Fu, Q. Peng, Q. Yao, X. Wang, A. Yu and Z. Chen, *Chem. Eng. J.*, 2020, **394**, 124822.

45 H. Luo, S. Dimitrov, M. Daboczi, J. S. Kim, Q. Guo, Y. Fang, M. A. Stoeckel, P. Samorì, O. Fenwick, A. B. J. Sobrido, X. Wang and M. M. Titirici, *ACS Appl. Nano Mater.*, 2020, **3**, 3371-3381.

46 G. Yu, J. Qian, P. Zhang, B. Zhang, W. Zhang, W. Yan and G. Liu, *Nat. Commun.*, 2019, **10**, 4912.

47 Y. Zhu, A. Marianov, H. Xu, C. Lang and Y. Jiang, *ACS Appl. Mater. Interfaces*, 2018, **10**, 9468-9477.

48 S. Li, J. Tan, Z. Jiang, J. Wang and Z. Li, *Chem. Eng. J.*, 2020, **384**, 123354.

49 M. Li, Y. Hu, G. Dong, T. Wu and D. Geng, *Small*, 2023, **19**, 2207242.